

# Geophysical Research Letters®



## RESEARCH LETTER

10.1029/2022GL100537

## First Lidar Profiling of Meteoric Ca<sup>+</sup> Ion Transport From ~80 to 300 km in the Midlatitude Nighttime Ionosphere

### Key Points:

- First lidar profiling of Ca<sup>+</sup> ions from ~80 to 300 km was made over Beijing in the nighttime ionosphere during geomagnetic quiet time
- Thermosphere-ionosphere Ca<sup>+</sup> layers (~10 s cm<sup>-3</sup>) are likely formed by uplifting ions from sporadic Ca<sup>+</sup> at ~110 km & show complex structures
- Spread F occurs concurrently with Thermosphere-ionosphere Ca<sup>+</sup> & strong sporadic E layers occur before the onset of TICa<sup>+</sup> and spread F, suggesting E- and F-region coupling

Jing Jiao<sup>1</sup> , Xinzhao Chu<sup>2</sup> , Han Jin<sup>1</sup> , Zelong Wang<sup>3</sup>, Yuchang Xun<sup>1,4</sup> , Lifang Du<sup>1</sup>, Haoran Zheng<sup>1</sup>, Fujun Wu<sup>1,5</sup> , Jiyao Xu<sup>1</sup> , Wei Yuan<sup>1</sup> , Chunxiao Yan<sup>1</sup> , Jihong Wang<sup>1</sup>, and Guotao Yang<sup>1</sup> 

<sup>1</sup>State Key Laboratory of Space Weather, National Space Science Center, Chinese Academy of Sciences, Beijing, China,

<sup>2</sup>Cooperative Institute of Research in Environmental Sciences & Department of Aerospace Engineering Sciences, University of Colorado Boulder, Boulder, CO, USA, <sup>3</sup>School of Science, Jiangsu University of Science and Technology, Zhenjiang, China, <sup>4</sup>College of Physics and Optoelectronics, Taiyuan University of Technology, Taiyuan, China, <sup>5</sup>School of Physics, Henan Normal University, Xinxiang, China

### Supporting Information:

Supporting Information may be found in the online version of this article.

### Correspondence to:

X. Chu and G. Yang,  
[xinzhao.chu@colorado.edu](mailto:xinzhao.chu@colorado.edu);  
[gyang@swl.ac.cn](mailto:gyang@swl.ac.cn)

### Citation:

Jiao, J., Chu, X., Jin, H., Wang, Z., Xun, Y., Du, L., et al. (2022). First lidar profiling of meteoric Ca<sup>+</sup> ion transport from ~80 to 300 km in the midlatitude nighttime ionosphere. *Geophysical Research Letters*, 49, e2022GL100537. <https://doi.org/10.1029/2022GL100537>

Received 21 JUL 2022

Accepted 13 SEP 2022

### Author Contributions:

**Conceptualization:** Jing Jiao, Xinzhao Chu, Han Jin, Guotao Yang

**Data curation:** Lifang Du, Haoran Zheng, Fujun Wu, Jiyao Xu, Wei Yuan, Chunxiao Yan, Jihong Wang, Guotao Yang

**Formal analysis:** Jing Jiao, Xinzhao Chu, Han Jin, Guotao Yang

**Funding acquisition:** Guotao Yang

**Investigation:** Jing Jiao, Xinzhao Chu, Han Jin, Yuchang Xun, Lifang Du, Fujun Wu, Jiyao Xu, Chunxiao Yan, Jihong Wang, Guotao Yang

**Abstract** We report a world record of lidar profiling of metallic Ca<sup>+</sup> ions up to 300 km in the midlatitude nighttime ionosphere during geomagnetic quiet time. Ca<sup>+</sup> measurements (~80–300 km) were made over Beijing (40.42°N, 116.02°E) with an Optical-Parametric-Oscillator-based lidar from March 2020 through June 2021. Main Ca<sup>+</sup> layers (80–100 km) persist through all nights, and high-density sporadic Ca<sup>+</sup> layers (~100–120 km) frequently occur in summer. Thermosphere-ionosphere Ca<sup>+</sup> (TICa<sup>+</sup>) layers (~110–300 km) are likely formed via Ca<sup>+</sup> uplifting from these sporadic layers. The lidar observations capture the complete evolution of TICa<sup>+</sup> layers from onset to ending, revealing intriguing features. Concurrent ionosonde measurements show strong sporadic E layers developed before TICa<sup>+</sup> and spread F onset. Neutral winds can partially account for observed vertical transport but enhanced electric fields are required to explain the results. Such lidar observations promise new insights into E- and F-region coupling and plasma inhomogeneities.

**Plain Language Summary** Inhomogeneities (also called irregularities) in the ionospheric plasma distribution can significantly degrade satellite communications and negatively impact Global Positioning System-based navigation systems that rely on the trans-ionospheric radio-wave propagation. Understanding the formation mechanisms of, thus predicting, ionospheric inhomogeneities is still a huge challenge in space weather research. Long-lived meteoric metal ions (>>1 day above 100 km altitude) converge to form dense ion layers, causing plasma irregularities in the ionosphere. Therefore, it is imperative to observe and understand the transport and formation of metallic ion layers. However, it is technically challenging to detect specific ion species, especially tracing ion transport over large vertical ranges and time durations. Numerous instruments detect electron density but cannot distinguish ion species. Rocket-borne mass spectrometers can distinguish ion species but provide only snapshots. Lidars provide a powerful tool to profile and trace metallic species over extended periods by exciting specific resonance fluorescence. The only metal ions detectable by ground-based lidars are Ca<sup>+</sup>, and previous lidar measurements reached ~180 km. Our Ca<sup>+</sup> lidar upgraded with narrowband lasers has achieved high detection sensitivity, enabling the Ca<sup>+</sup> profiling up to 300 km. Such lidar measurements of dynamical Ca<sup>+</sup> layers open a new window to study plasma irregularities.

## 1. Introduction

Active metallic species (e.g., Fe, Mg, Na, K, Li, Ca, Ni, and Al) exist in the Earth's upper atmosphere (Plane et al., 2015). They are released from interplanetary dust particles (also called cosmic dust) via ablation and sputtering (Plane, 2012) with the major meteoroid source being the Jupiter Family of Comets (Carrillo-Sánchez et al., 2016, 2020; Huang et al., 2015). The released meteoric metal atoms and ions undergo complex processes over multiple temporal and spatial scales and form various metal layers (e.g., Bishop & Earle, 2003; Chu et al., 2011, 2020; Mathews, 1998; Plane, 2003). Using the main (permanent) metal layers (~80–105 km) as tracers, resonance-fluorescence lidars have become one of the most powerful tools for studying cosmic dust and understanding the thermal structures, chemistry, and dynamics in the mesosphere and lower thermosphere (e.g., Chu & Papen, 2005).

Above the main metal layers, thermosphere-ionosphere metal (TIMt) layers were recently discovered in Antarctica (Chu et al., 2011) and then detected globally with lidars up to ~200 km (e.g., Chu et al., 2020, 2021; Friedman

© 2022. The Authors.

This is an open access article under the terms of the [Creative Commons Attribution License](https://creativecommons.org/licenses/by/4.0/), which permits use, distribution and reproduction in any medium, provided the original work is properly cited.

**Methodology:** Jing Jiao, Xinzhao Chu, Han Jin, Guotao Yang  
**Project Administration:** Guotao Yang  
**Resources:** Lifang Du, Haoran Zheng, Fujun Wu, Jiyao Xu, Wei Yuan, Chunxiao Yan, Jihong Wang, Guotao Yang  
**Software:** Jing Jiao, Han Jin  
**Supervision:** Xinzhao Chu, Han Jin, Guotao Yang  
**Validation:** Jing Jiao, Xinzhao Chu, Han Jin, Guotao Yang  
**Visualization:** Jing Jiao  
**Writing – original draft:** Jing Jiao, Xinzhao Chu, Han Jin  
**Writing – review & editing:** Xinzhao Chu, Han Jin, Zelong Wang, Yuchang Xun, Lifang Du, Jiyao Xu, Wei Yuan, Guotao Yang

et al., 2013; Gao et al., 2015; Raizada et al., 2020; Tsuda et al., 2015; Xun et al., 2019). Following the terminology in Chu et al. (2020, 2021), we use TIMt and TIMt<sup>+</sup> to represent the neutral and ionized TIMt layers, respectively, and name such layers of the Fe, Na, K, and Ca<sup>+</sup> species as TIFe, TINa, TIK, and TICa<sup>+</sup> layers. Antarctic lidar observations have revealed TIFe layers with clear gravity wave signatures and one-to-one correlation with auroral activity (Chu et al., 2011, 2020). A TIFe model by Chu and Yu (2017) replicated a TIFe event on 28 May 2011, based on the hypothesis that neutral TIFe layers are produced through neutralization of converged TIFe<sup>+</sup> layers via direct recombination ( $Fe^+ + e^- \rightarrow Fe + hv$ ). These TIFe<sup>+</sup> ions are transported upward from the main deposition region to ~500 km (the model top) and converged by both polar electric field and gravity-wave-induced neutral winds (Chu & Yu, 2017). This example demonstrates that TIMt and TIMt<sup>+</sup> layers provide new possibilities for lidar investigation of the fundamental space-atmosphere interactions, especially in the E and F regions.

Metallic ions are the major composition of sporadic E layers (e.g., Kopp, 1997) and can interfere with satellite communications and navigations that rely on the trans-ionospheric radio-wave propagation. E- and F-region coupling further complicates the ion transport and layering, making the prediction of ionospheric irregularities extremely challenging (e.g., Huba et al., 2019, 2020; Makela & Otsuka, 2012). Comprehensive observations and modeling efforts are essential to advance our understanding of ionospheric irregularities. Metallic ions have been observed by satellites in the F region, like Fe<sup>+</sup> (e.g., Grebowsky & Brinton, 1978; Hanson & Sanatani, 1971), Mg<sup>+</sup>, and Ca<sup>+</sup> (e.g., Gardner et al., 1999; Scharringhausen, 2007), but suffer low resolutions. Ionosondes and radars detect total electron density but cannot distinguish ion species. Rocket-borne spectrometers can distinguish ion species but provide only snapshots (e.g., Grebowsky & Aikin, 2002; Istomin, 1963; Roddy et al., 2004, 2007). Lidar can distinguish and trace metallic species by exciting resonance fluorescence, but Fe<sup>+</sup> and Mg<sup>+</sup> requiring short UV wavelengths to excite are out of reach from the ground due to atmospheric absorption.

Ca<sup>+</sup> ions are the only metallic ion species detectable by ground-based instruments. Since the first detection of Ca<sup>+</sup> in twilight spectrum by Vallance-Jones (1956), ground-based twilight observations of Ca<sup>+</sup> have been made up to 280-km shadow height (Broadfoot, 1967). However, lidar detection of Ca<sup>+</sup> has been limited to ~180 km (e.g., Ejiri et al., 2019; Gardner et al., 1993; Gerding et al., 2000; Granier et al., 1985; Raizada et al., 2011, 2012, 2020) until this study. Here we report an extraordinary record of lidar profiling of TICa<sup>+</sup> layers up to ~300 km, reaching above the F region peak. The observations were made over Beijing, China and reveal a high occurrence of TICa<sup>+</sup> being uplifted rapidly from ~110 to 300 km around midnight in the summer. Along with the concurrent and nearby observations of sporadic E layers and spread F with an ionosonde and of neutral winds with a Fabry-Perot interferometer (FPI), such lidar measurements of TICa<sup>+</sup> layers open a new window to explore ion transport, E–F region coupling, and ionospheric irregularities at midlatitudes.

## 2. Observations With High-Sensitivity Ca<sup>+</sup>/Ca Lidar Over Beijing

The Ca<sup>+</sup> measurements were made with an upgraded resonance-fluorescence dual-wavelength Ca<sup>+</sup>/Ca lidar at Yanqing Station (40.42°N, 116.02°E) near Beijing. Two broadband pulsed dye lasers employed in the original Ca<sup>+</sup>/Ca lidar system (Wu et al., 2020) were replaced with two solid-state, injection-seeded, and pulsed Optical Parametric Oscillator (OPO) lasers in March 2020. The two OPO lasers were tuned to wavelengths of 393.4777 and 422.7918 nm (in vacuum) for exciting resonance fluorescence of Ca<sup>+</sup> and Ca, respectively. Because of the narrow bandwidth (with the full-width-at-half-maximum less than 200 MHz) and relatively high pulse energy (30 mJ per pulse at 15 Hz repetition rate) of the OPO lasers, the signal-to-noise ratios of the return photon counts were significantly improved from that of the original system. In order to detect Ca<sup>+</sup> ions higher into the F<sub>2</sub> region, the maximum altitude of the lidar detection range was increased to 393 km. The Ca<sup>+</sup> data used in this paper were taken from March 2020 to June 2021 with the raw time resolution of 33 s and vertical resolution of 96 m.

Figure 1 shows four representative nights of Ca<sup>+</sup> number density measurements versus universal time and altitude from 80 to 300 km. Note that 16.265 UT is the local midnight at Yanqing. The main Ca<sup>+</sup> layers distribute below 100 km and persist throughout the observations. Sporadic Ca<sup>+</sup> layers with high densities occur around ~100–120 km with some height and density variations through the observations. TICa<sup>+</sup> layers occur between the sporadic Ca<sup>+</sup> and up to ~300 km. The most likely process is that Ca<sup>+</sup> ions start to rise from the sporadic Ca<sup>+</sup> layers roughly 2–0 hr before the local midnight (i.e., ~14–16 UT), and are transported into the F<sub>1</sub> and F<sub>2</sub> regions, forming the TICa<sup>+</sup> layers up to 300 km. The TICa<sup>+</sup> layers on these four nights exhibit the “up-down-up-down” or “up-down” structures, which resemble “M” or “Λ” shapes. Eventually, the TICa<sup>+</sup> layers are transported downward and merge with sporadic Ca<sup>+</sup> layers around 140 to 120 km at roughly 2–4 hr after the midnight. These

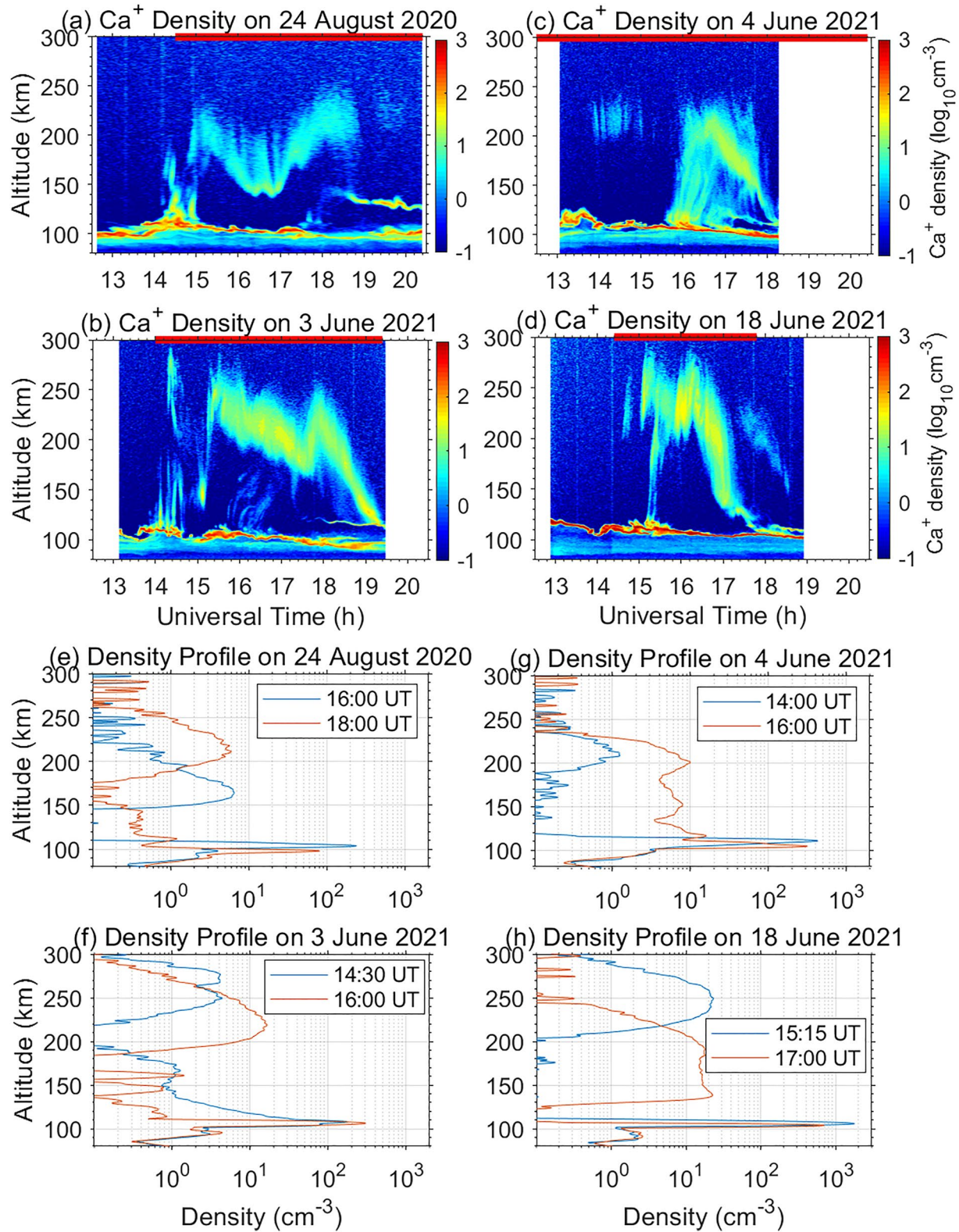


**Figure 1.** Lidar observations of Ca<sup>+</sup> layers from 80 to 300 km at Yanqing. (a–d) Ca<sup>+</sup> densities in log-10 scale as a function of universal time and altitude on 24 August 2020, 3, 4, and 18 June 2021. A Hamming window with a full-width-at-half-maximum of 960 m and 165 s was used to smooth and oversample the data at the original lidar resolution of 96 m and 33 s. The red bars on top of contour figures represent the spread F periods. (e–h) Vertical profiles of Ca<sup>+</sup> densities at select times.

observations basically capture the evolution process from the onset to the ending of  $\text{TICa}^+$  layers. Besides the major  $\text{TICa}^+$  in “M” or “A” shapes, there are some peculiar features like the nearly vertical structures from  $\sim 110$  to  $\sim 300$  km around 14UT on 3 June 2021, and the interference-fringe-like pattern from 200 to 250 km during 14–15UT on 4 June 2021. Many detailed features of the ion transport and layering structures shown in Figure 1 have never been observed before.

Vertical profiles of  $\text{Ca}^+$  ions at select times are plotted in Figures 1e–1h. Excluding the sporadic  $\text{Ca}^+$  layers, the  $\text{TICa}^+$  densities range roughly from  $\sim 0.3$  to  $10\text{s cm}^{-3}$ , comparable to or even larger than that of the main  $\text{Ca}^+$  layers below 100 km. Sporadic  $\text{Ca}^+$  layers appearing as sharp peaks mainly between 90 and 120 km are “persistent” through all four nights, with peak densities ranging from  $\sim 100$  to nearly  $2,000\text{ cm}^{-3}$ . A second sporadic  $\text{Ca}^+$  layer appears later in the nights when  $\text{TICa}^+$  descends to  $\sim 140$  to 120 km (Figures 1a–1d). Figure 1 contours also exhibit high-frequency wave features with periods of  $\sim 10$  min, for example, the upward and downward phase progression on 4 June 2021 during  $\sim 16$ –18UT. Such “up-down”  $\text{TICa}^+$  shapes are quite similar to the  $\text{TIFe}^+$  contours simulated by Chu and Yu (2017).

To quantify the evolution of  $\text{Ca}^+$  at different altitudes, the time series of column abundances are plotted in Figure 2 for the lower and upper regions. In the lower region (80–140 km), the  $\text{Ca}^+$  column abundance varies from  $0.5 \times 10^8$  to  $2 \times 10^9\text{ cm}^{-2}$ . In the upper region (140–300 km), the  $\text{Ca}^+$  column abundance varies from 0 to  $2.6 \times 10^8\text{ cm}^{-2}$ . A general trend is that the upper-region column abundance increases with the reduction of the lower-region column abundance, as shown within the red rectangles in Figure 2, when  $\text{TICa}^+$  are the dominant features in the F region. Such anti-correlations support a hypothesis that  $\text{Ca}^+$  ions in the  $\text{TICa}^+$  layers are transported upward from the lower altitude region where sporadic  $\text{Ca}^+$  and E layers reside.

### 3. Concurrent Lidar and Ionosonde Observations

The ion transport from the E to F regions and  $\text{TICa}^+$  layers shown above occur near the midnight on geomagnetic quiet days under the low solar activity conditions, according to the solar flux F10.7 and geomagnetic Kp and Dst indices tabulated in Table S1 of Supporting Information S1. Although being a minor species,  $\text{Ca}^+$  ions are used to represent all metallic ion species. As metallic ions are the major composition of sporadic E, we examine the concurrent ionosonde measurements made at Shisanling Station ( $40.3^\circ\text{N}$ ,  $116.2^\circ\text{E}$ ),  $\sim 28$  km away from Yanqing Station. Indeed, sporadic E layers were observed at the same time and altitudes as sporadic  $\text{Ca}^+$  layers (90–120 km), and spread F occurred over the same time as  $\text{TICa}^+$  layers. The lidar and ionosonde observations on 3 June 2021 are shown as an example in Figure 3.

The ionosonde (DPS-4d) at Shisanling takes one ionogram every 15 min. Sporadic E layers were observed through the whole night (see  $h'Es$  in Figure 3c), corresponding to the sporadic  $\text{Ca}^+$  layers around 110 km (Figure 3a). The critical frequency ( $f_oEs$ ) was over 5 MHz at 12UT. After a short period of decrease, the  $f_oEs$  increased to  $\sim 9$  MHz at 13:15UT and stayed high for about half an hour before dropping sharply to  $\sim 3$  MHz at 14UT (Figure 3c). These changes in  $f_oEs$  mean changes in electron density. This sharp drop of  $f_oEs$  corresponded to a sharp increase of  $\sim 80$  km for the bottom height of the F layer ( $h'F$ ) and  $\sim 40$  km for the peak height of the  $F_2$  layer ( $hmF_2$ ). Spread F and the uplift of  $\text{TICa}^+$  ions started to occur in the ionograms (Figure S2 in Supporting Information S1) and in the lidar contour (Figure 3a) around the same time ( $\sim 14$ UT). The occurrence period of spread F is marked as a red bar on the top of Figure 3a, overlapping the  $\text{TICa}^+$  occurrence from the onset to the ending ( $\sim 14$ –19.5UT). Sample ionograms with strong sporadic E and spread F are shown in Figures 3d and 3e, respectively. As the  $\text{TICa}^+$  layer descends from the F to E region and merges with a sporadic E layer, the spread F weakens and then disappears from the ionogram at  $\sim 19$ UT (see Figure S2 in Supporting Information S1).

The vertical transport velocities for the “M” structures of  $\text{TICa}^+$  layers from 15 to 19.2UT are about +140,  $-8.5$ , +81, and  $-26$  m/s, respectively. Besides this M-shape main structure, the  $\text{TICa}^+$  layers between 14 and 15UT are nearly vertical with periodic structures at a period of  $\sim 10$  min, while the structures between 15.6 and 16.8UT below “M” look like “overturning” features. Many of these characteristics are eye opening and have raised significant questions on ion transport and layering mechanisms, including the large vertical transport velocities.

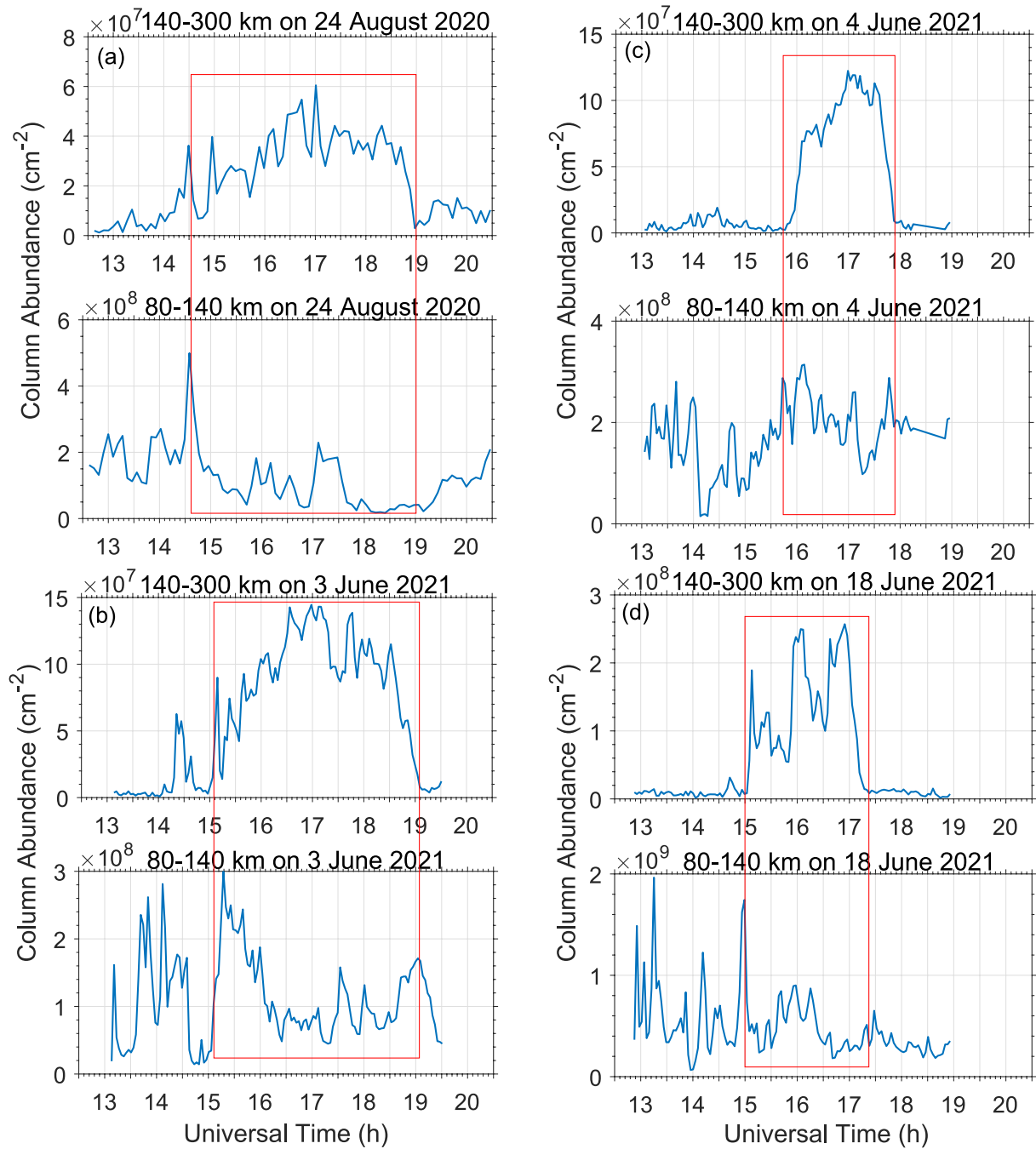


**Figure 2.** Comparison between column abundances of  $\text{Ca}^+$  ions in the altitude ranges of 140–300 km and 80–140 km (including sporadic  $\text{Ca}^+$ ) for four observational nights.

#### 4. Discussion

The continuity equation given in the TIMt modeling study by Chu and Yu (2017) can be utilized to study metallic ions ( $\text{M}^+$ ) including  $\text{Ca}^+$ :

$$\frac{\partial N_{\text{M}^+}}{\partial t} = S + Q - L - \nabla \cdot (N_{\text{M}^+} \vec{V}_{\text{M}^+}) \quad (1)$$

where  $S$  represents the external sources from direct meteoric deposition of  $\text{M}^+$  via collisional ionization during meteor ablation,  $Q$  is the chemical production of  $\text{M}^+$  via charge transfer with  $\text{NO}^+$  and  $\text{O}_2^+$  ions, photoionization,

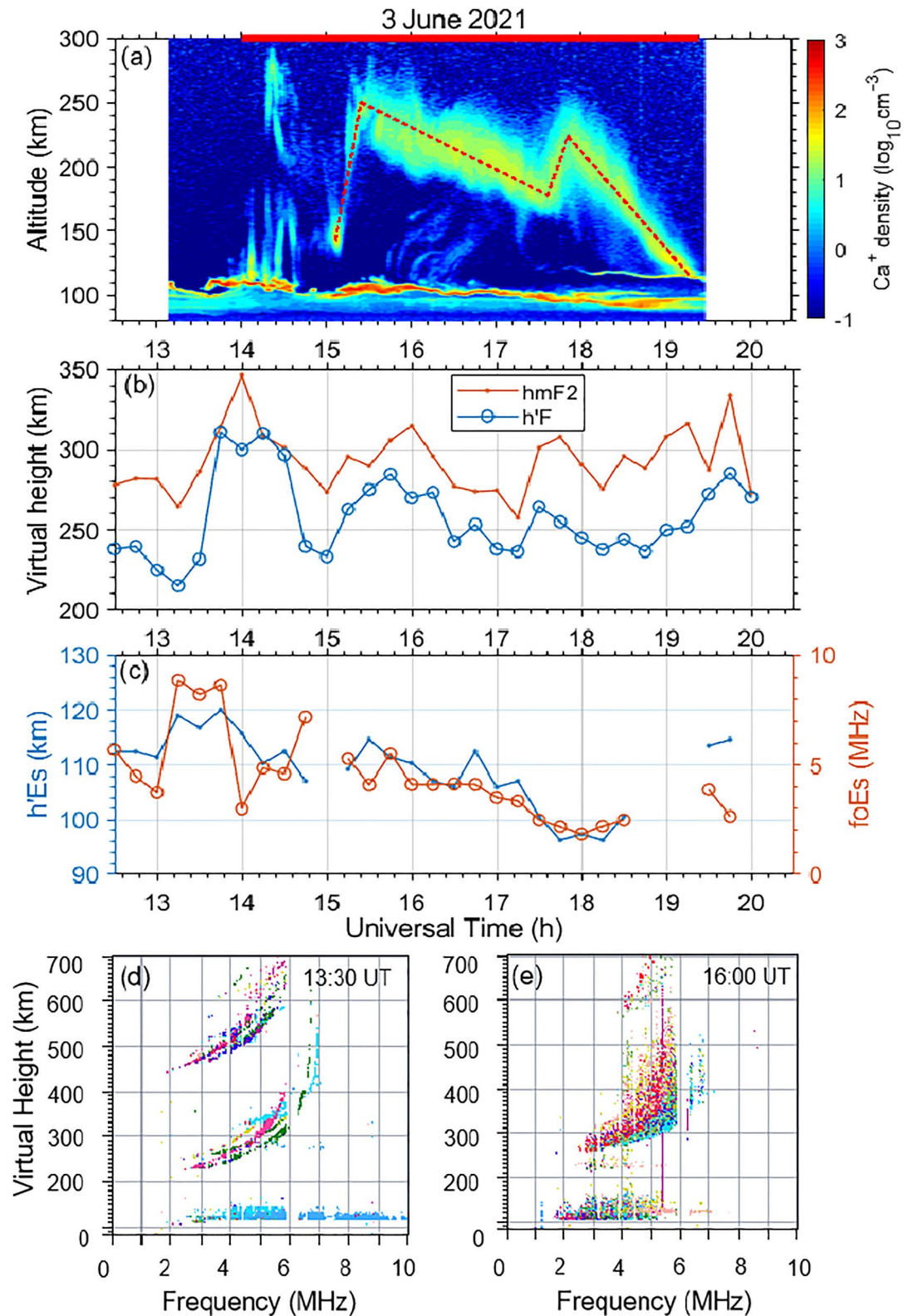


**Figure 3.** Concurrent lidar and ionosonde observations of Ca<sup>+</sup> on 3 June 2021. (a) Contour of Ca<sup>+</sup> density measured by lidar at Yanqing. Dashed lines mark the phase lines that are used to calculate vertical transport velocities of TICa<sup>+</sup> layers. (b) Time series of ionospheric F-layer heights, where hmF2 is the peak height of the F<sub>2</sub> layer, and h'F is the bottom height of the F layer. (c) Time series of the virtual height (h'Es) and critical frequency (foEs) of sporadic E layers. (d and e) Select ionograms from Shisanling showing sporadic E and spread F, respectively.

and dissociative release, and  $L$  is the chemical loss of  $Mt^+$  via direct recombination with electrons and reactions with  $O_3$ ,  $N_2$ ,  $CO_2$ , and  $H_2O$  molecules (Plane et al., 2018). The last term in 1 is the vertical and horizontal transport of  $Mt^+$  ions (Chu & Yu, 2017). Note that  $Mt^+$  ions can survive long-range and long-duration transport because of their long lifetime (Plane, 2003). In the E and F regions above  $\sim 110$  km, the chemical loss of  $Mt^+$  is negligible due to diminished concentrations of  $O_3$ ,  $N_2$ , and  $CO_2$  and the fact that direct recombination converts only  $\sim 0.1\%$  of  $Mt^+$  ions to neutral atoms (Chu & Yu, 2017). Chemical production of  $Mt^+$  in the F region is also small in the midlatitude night because of the absence of sunlight for photoionization and the lack of neutral metal atoms for charge transfer. Therefore, external sources and transport are the two major factors shaping TIMt<sup>+</sup> layers in the E–F regions.

No permanent  $Mt^+$  layers exist above the main meteoric deposition region ( $\sim 80$ – $115$  km), (e.g., Carrillo-Sánchez et al., 2016; Chu & Yu, 2017; Plane, 2003; Plane et al., 2015).  $Mt^+$  ions that reach the  $F_2$  region must have been transported from elsewhere. Ultimately, F-region TIMt<sup>+</sup> ions are transported from below as the  $Mt^+$  sources are located in the D–E regions, but the actual transport processes for a particular site can be complicated. Carter and Forbes (1999) have demonstrated that the equatorial fountain effect can transport  $Mt^+$  to very high altitudes (over 1,000 km) via  $\overline{E} \times \overline{B}$  drift during the day, and then the  $Mt^+$  ions diffuse poleward and downward along geomagnetic field lines to low- and mid-latitude F–E regions in the night. This transport mechanism was used to explain the observations of sporadic E and TIMt layers at Arecibo (Carter & Forbes, 1999; Friedman et al., 2013) and Lijiang (Gao et al., 2015). However, the geomagnetic latitude of Beijing ( $\sim 35^\circ N$ ) is much higher than Arecibo and Lijiang, and fountain effects on the four nights were not strong (see Supporting Information S1). Thus, fountain effects would unlikely impact Beijing on these nights. At high latitudes, strong polar electric fields and wave-induced neutral winds can transport ions upward but these ions are unlikely to reach Beijing, especially during geomagnetic quiet days as shown here (Bristow & Watkins, 1991; Chu & Yu, 2017; MacDougall et al., 2000; Nygren et al., 1984). After ruling out long-range transport from low or high latitudes, we hypothesize that most of the TICa<sup>+</sup> layers observed at Beijing are vertically transported from the midlatitude E and/or D regions over or near Beijing. Certainly, short-range horizontal advection of a Ca<sup>+</sup> cloud over the vertical-pointing lidar beam could play a minor role, which might explain some peculiar features, such as the isolated pattern during 14–15UT on 4 June 2021. This regional vertical-transport hypothesis is supported by the anti-correlation of column abundances between the upper TICa<sup>+</sup> and sporadic Ca<sup>+</sup> ions as shown in Figure 2—the increase of TICa<sup>+</sup> corresponds with the loss of Ca<sup>+</sup> in the E region.

Vertical ion transport is mainly driven by electric fields, neutral winds, gravitational force, and diffusion (Chu & Yu, 2017). We examine how two major factors, neutral winds and electric fields, impact the  $Mt^+$  transport. The vertical drift velocity induced by neutral winds is given in Chu and Yu (2017):

$$v_{izw} = \frac{\xi \cos \theta_D}{1 + \xi^2} V_{n,x} - \frac{\sin(2\theta_D)}{2(1 + \xi^2)} V_{n,y} + \left(1 - \frac{\cos^2 \theta_D}{1 + \xi^2}\right) V_{n,z} \quad (2)$$

where  $\theta_D$  is the dip angle of geomagnetic field line ( $\theta_D = 64.34^\circ$  at Beijing),  $\xi$  is the ratio of ion-neutral collision frequency to the gyro frequency of ions, and  $V_n$  is the neutral winds in geomagnetic zonal (x), meridional (y), and vertical (z) coordinates (Chu et al., 2021). Neutral winds at altitudes of 250, 96, and 87 km were concurrently measured with a FPI from three airglow emission wavelengths (OI 630.0, OI 557.7, and OH 892.0 nm) at Xinglong Station ( $40.23^\circ N$ ,  $117.34^\circ E$ ) (Yuan et al., 2010),  $\sim 130$  km away from Yanqing. The meridional winds at 250 km were southward with a maximum of approximately  $-100$  m/s through the observational nights (Figure 4). The vertical Ca<sup>+</sup> drift velocity at 250 km, calculated from both the meridional and zonal winds using the equation above, was upward, in the range of 0–50 m/s (Figure 4), and largely driven by the meridional winds.

The calculated vertical drift velocities suggest that the neutral winds alone cannot account for the large vertical transport velocities of 80–140 m/s observed by the Ca<sup>+</sup> lidar, if the FPI winds at 250 km are assumed to represent the neutral winds from 110 to 300 km. It is therefore necessary to consider the electric-field-induced transport. Two major sources generating the electric fields at midlatitudes are the neutral wind dynamo and penetration of high-latitude convective electric fields (Kelley, 2009). As Beijing is well below the sub-aurora zone, penetration electric fields are most likely ineffective. Under normal conditions, the midlatitude electric fields (e.g., Buonsanto et al., 1993; Kelley, 2009) are only a few mV/m, which are much smaller than the 10s mV/m fields in the polar regions. As gravity reduces effects of the upward vertical ion drift, only neutral winds and F-region dynamo electric fields unlikely produce the fast vertical transport observed.

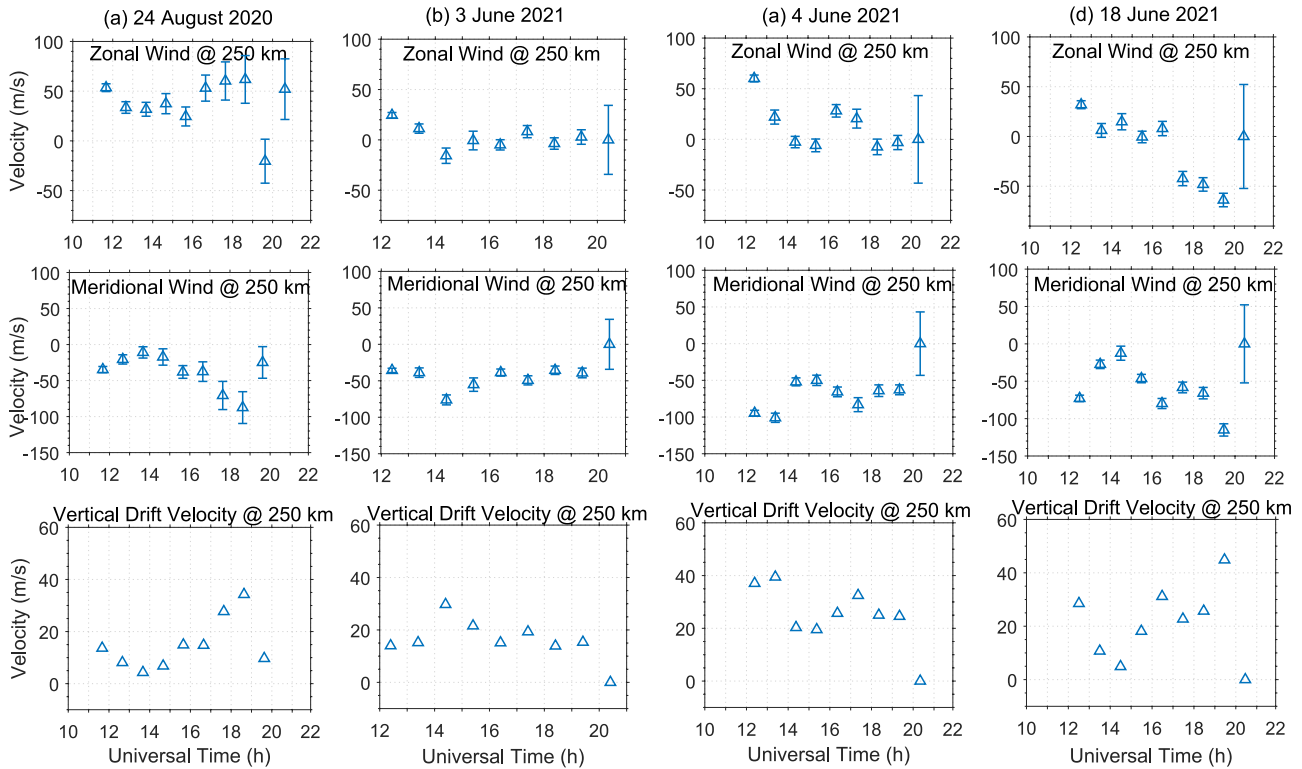


**Figure 4.** Time series of zonal (top) and meridional (middle) neutral winds at 250 km measured by Fabry-Perot interferometer at Xinglong. (bottom) Vertical drift velocities of  $\text{Ca}^+$  ions calculated using Equation 2 on 24 August 2020, 3, 4, and 18 June 2021 in (a–d), respectively.

However, two special conditions were present during the nights of  $\text{TICa}^+$  occurrence. One was the occurrence of strong sporadic E before the onset of  $\text{TICa}^+$  and spread F, and another was the presence of high-frequency gravity waves (seen as periodic features in Figure 1). Electric fields generated by the Hall polarization processes in a midlatitude sporadic E layer, that is, the so-called Es-layer instability mechanism (Cosgrove & Tsunoda, 2002, 2003; Haldoupis et al., 1996; Tsunoda, 1998), could map to the F region, causing positive feedback and enhancing polarization electric fields (Kelley et al., 2003; Makela & Otsuka, 2012; Tsunoda & Cosgrove, 2001). Such electrodynamic coupling between the E and F regions, which increases the growth rate of Perkins instability (Perkins, 1973), was modeled successfully to explain midlatitude medium-scale traveling ionospheric disturbance (MSTIDs) (Yokoyama et al., 2009; Yokoyama & Hysell, 2010). Gravity waves can introduce large vertical and/or horizontal winds in the E and F regions which can transport ions as demonstrated in the TIFe model simulations (Chu & Yu, 2017). Furthermore, gravity waves can provide seeding sources and help amplify the growth rate of Perkins instability (Huang et al., 1994; Kelley & Fukao, 1991; Wei et al., 2021). We hypothesize that the combination of these factors, that is, the Perkins instability, sporadic E-layer instability mechanism, and gravity wave seeding mechanism, together with neutral winds in the E and F regions may transport ions effectively from the E to F regions, leading to the observed fast development of spread F and  $\text{TICa}^+$  layers. The occurrence of  $\text{TICa}^+$  over Beijing that peaks in May to August under low solar fluxes is consistent with the most frequent occurrence of mid-latitude sporadic E, spread F, and MSTIDs between May and August in Asia (Bowman, 1996; Ding et al., 2011; Haldoupis et al., 2007; Huang et al., 2011). Further considering that virtual heights  $h_m F_2$  and  $h'F$  showed three “jumps” corresponding to three fast uplifts of  $\text{TICa}^+$  layers around 14, 15, and 17.5 UT in Figure 3b and Figure S5 in Supporting Information S1, the idea that polarization electric fields associated with coupling between MSTIDs and sporadic E are responsible for  $\text{TICa}^+$  uplifts is supported by the current data. Certainly, this hypothesis needs to be tested via numerical modeling and coordinated observations in the future.

## 5. Conclusions

A world record of lidar profiling of metallic  $\text{Ca}^+$  layers up to  $\sim 300$  km, reaching over the F region peak, has been made over Beijing during solar and geomagnetic quiet time. Such measurements were enabled by an OPO-based

narrowband Ca<sup>+</sup> lidar. The lidar observations have captured the complete evolution process of TICA<sup>+</sup> layers from onset to ending. Ca<sup>+</sup> ions are uplifted from strong sporadic Ca<sup>+</sup> layers residing at ~110 km shortly before or right around midnight and transported into the F region, forming TICA<sup>+</sup> layers up to ~300 km. The TICA<sup>+</sup> layers then move up and down with varying vertical transport velocities. Approximately 2 and 3 hr after midnight, the TICA<sup>+</sup> layers descend quickly and finally merge with another sporadic E layer at ~140 km. The high-resolution data also reveal gravity wave features with short periods (~10 min) and large vertical wavelengths, and some TICA<sup>+</sup> layers exhibit nearly vertical phase lines. Spread F occurred concurrently with TICA<sup>+</sup> layers, and strong sporadic E layers occurred before the onset of TICA<sup>+</sup> and spread F.

Such lidar profiling and tracking of metallic Ca<sup>+</sup> ions, over large altitude ranges and extended observational periods, reveal intriguing features that have never been observed before but are linked to plasma irregularities, ion transport, and E–F region coupling. The concurrent lidar, ionosonde, and FPI observations provide evidence that regional vertical ion transport from the D–E to the F region plays the major role in forming TICA<sup>+</sup> layers, which represent other metallic ions and plasma irregularities, in the midlatitude nighttime ionosphere. The fast vertical transport velocities can likely be explained by a combination of neutral winds and enhanced electric fields that are produced via electrodynamic coupling between the E and F regions involving Es-layer instability and gravity wave seeding mechanisms of Perkins instability. Certainly, future numerical modeling and coordinated observations are necessary to test these hypotheses and help understand ion transport and plasma irregularity formation, which are important factors in space weather research.

### Data Availability Statement

The ionosonde data were provided by Beijing National Observatory of Space Environment, Institute of Geology and Geophysics, Chinese Academy of Sciences through the Geophysics Center, National Earth System Scientific Data Center (<http://wdc.geophys.ac.cn>). The data shown in this work can be downloaded from Zenodo repository (Jiao et al., 2022, <https://doi.org/10.5281/zenodo.7020759>).

### Acknowledgments

The authors thank Ian Geraghty and Jackson Jandreau for English editing and thank Dr. Shun-Rong Zhang, Dr. Zhibin Yu, and Yingfei Chen for intriguing discussions. This work was supported by the Youth Innovation Promotion Association of Chinese Academy of Sciences (2019150), Project of Stable Support for Youth Team in Basic Research Field, Chinese Academy of Sciences (Grant No. YSBR-018), NSFC (42004134, 41627804), Chinese Meridian Project, and Pandeng Program of National Space Science Center, Chinese Academy of Sciences. XC was partially supported by USA National Science Foundation grants OPP-1443726, OPP-2110428, and AGS-1452351.

### References

- Bishop, R. L., & Earle, G. D. (2003). Metallic ion transport associated with midlatitude intermediate layer development. *Journal of Geophysical Research*, 108(A1), SIA3-1–SIA3-8. <https://doi.org/10.1029/2002JA009411>
- Bowman, G. G. (1996). Periodicities and spread-F associated with large-scale travelling ionospheric disturbances. *Indian Journal of Radio and Space Physics*, 25, 93–100.
- Bristow, W. A., & Watkins, B. J. (1991). Numerical simulation of the formation of thin ionization layers at high latitudes. *Geophysical Research Letters*, 18(3), 404–407. <https://doi.org/10.1029/90GL02588>
- Broadfoot, A. L. (1967). Twilight Ca<sup>+</sup> emission from meteor trails up to 280 km. *Planetary and Space Science*, 15(3), 503–514. [https://doi.org/10.1016/0032-0633\(67\)90159-6](https://doi.org/10.1016/0032-0633(67)90159-6)
- Buonsanto, M. J., Hagan, M. E., Salah, J. E., & Fejer, B. G. (1993). Solar cycle and seasonal variations in F region electrodynamics at Millstone Hill. *Journal of Geophysical Research*, 98(A9), 15677–15683. <https://doi.org/10.1029/93JA01187>
- Carrillo-Sánchez, J. D., Gómez-Martin, J. C., Bones, D. L., Nesvorný, D., Pokorný, P., Benna, M., et al. (2020). Cosmic dust fluxes in the atmospheres of Earth, Mars, and Venus. *Icarus*, 335, 113395. <https://doi.org/10.1016/j.icarus.2019.113395>
- Carrillo-Sánchez, J. D., Nesvorný, D., Pokorný, P., Janches, D., & Plane, J. M. C. (2016). Sources of cosmic dust in the Earth's atmosphere. *Geophysical Research Letters*, 43(23), 11979–18679. <https://doi.org/10.1002/2016GL071697>
- Carter, L. N., & Forbes, J. M. (1999). Global transport and localized layering of metallic ions in the upper atmosphere. *Annales Geophysicae*, 17(2), 190–209. <https://doi.org/10.1007/s00585-999-0190-6>
- Chu, X., Chen, Y., Cullens, C. Y., Yu, Z., Xu, Z., Zhang, S.-R., et al. (2021). Mid-latitude thermosphere-ionosphere Na (TINa) layers observed with high-sensitivity Na Doppler lidar over Boulder (40.13°N, 105.24°W). *Geophysical Research Letters*, 48(11), e2021GL093729. <https://doi.org/10.1029/2021GL093729>
- Chu, X., Nishimura, Y., Xu, Z., Yu, Z., Plane, J. M. C., Gardner, C. S., & Ogawa, Y. (2020). First simultaneous lidar observations of thermosphere-ionosphere Fe and Na (TlFe and TINa) layers at McMurdo (77.84°S, 166.67°E), Antarctica with concurrent measurements of aurora activity, enhanced ionization layers, and converging electric field. *Geophysical Research Letters*, 47(20), e2022GL100397. <https://doi.org/10.1029/2020GL090181>
- Chu, X., & Papen, G. C. (2005). Resonance fluorescence lidar for measurements of the middle and upper atmosphere. In T. Fujii & T. Fukuchi (Eds.), *Laser remote sensing* (pp. 179–432). CRC Press, Taylor and Francis.
- Chu, X., & Yu, Z. (2017). Formation mechanisms of neutral Fe layers in the thermosphere at Antarctica studied with a thermosphere-ionosphere Fe/Fe<sup>+</sup> (TlFe) model. *Journal of Geophysical Research: Space Physics*, 122, 6812–6848. <https://doi.org/10.1002/2016JA023773>
- Chu, X., Yu, Z., Gardner, C. S., Chen, C., & Fong, W. (2011). Lidar observations of neutral Fe layers and fast gravity waves in the thermosphere (110–155 km) at McMurdo (77.8°S, 166.7°E), Antarctica. *Geophysical Research Letters*, 38(23), L23807. <https://doi.org/10.1029/2011GL050016>
- Cosgrove, R. B., & Tsunoda, R. T. (2002). A direction-dependent instability of sporadic-E layers in the nighttime midlatitude ionosphere. *Geophysical Research Letters*, 29(18), 11-1–11-4. <https://doi.org/10.1029/2002GL014669>
- Cosgrove, R. B., & Tsunoda, R. T. (2003). Simulation of the nonlinear evolution of the sporadic-E layer instability in the nighttime midlatitude ionosphere. *Journal of Geophysical Research*, 108(A7), 1283. <https://doi.org/10.1029/2002JA009728>

- Ding, F., Wan, W., Xu, G., Yu, T., Yang, G., & Wang, J. (2011). Climatology of medium-scale traveling ionospheric disturbances observed by a GPS network in central China. *Journal of Geophysical Research*, *116*, A09327. <https://doi.org/10.1029/2011JA016545>
- Ejiri, M. K., Nakamura, T., Tsuda, T. T., Nishiyama, T., Abo, M., Takahashi, T., et al. (2019). Vertical fine structure and time evolution of plasma irregularities in the Es layer observed by a high-resolution Ca<sup>+</sup> lidar. *Earth Planets and Space*, *71*(1), 1–10. <https://doi.org/10.1186/s40623-019-0984-z>
- Friedman, J. S., Chu, X., Brum, C. G. M., & Lu, X. (2013). Observation of a thermospheric descending layer of neutral K over Arecibo. *Journal of Atmospheric and Solar-Terrestrial Physics*, *104*, 253–259. <https://doi.org/10.1016/j.jastp.2013.03.002>
- Gao, Q., Chu, X., Xue, X., Dou, X., Chen, T., & Chen, J. (2015). Lidar observations of thermospheric Na layers up to 170 km with a descending tidal phase at Lijiang (26.7°N, 100.0°E), China. *Journal of Geophysical Research: Space Physics*, *120*, 9213–9220. <https://doi.org/10.1002/2015JA021808>
- Gardner, C. S., Kane, T. J., Senft, D. C., Qian, J., & Papen, G. C. (1993). Simultaneous observations of sporadic E, Na, Fe, and Ca<sup>+</sup> layers at Urbana, Illinois: Three case studies. *Journal of Geophysical Research*, *98*(D9), 16865–16873. <https://doi.org/10.1029/93JD01477>
- Gardner, J. A., Broadfoot, A. L., McNeil, W. J., Lai, S. T., & Murad, E. (1999). Analysis and modeling of the GLO-1 observations of meteoric metals in the thermosphere. *Journal of Atmospheric and Solar-Terrestrial Physics*, *61*(7), 545–562. [https://doi.org/10.1016/S1364-6826\(99\)00013-9](https://doi.org/10.1016/S1364-6826(99)00013-9)
- Gerding, M., Alpers, M., Von Zahn, U., Rollason, R. J., & Plane, J. M. C. (2000). Atmospheric Ca and Ca<sup>+</sup> layers: Midlatitude observations and modeling. *Journal of Geophysical Research*, *105*(A12), 27131–27146. <https://doi.org/10.1029/2000JA900088>
- Granier, G., Jégou, J. P., & Mégie, G. (1985). Resonant lidar detection of Ca and Ca<sup>+</sup> in the upper atmosphere. *Geophysical Research Letters*, *12*(10), 655–658. <https://doi.org/10.1029/GL012101p00655>
- Grebowsky, J. M., & Aikin, A. C. (2002). In situ measurements of meteoric ions. *Meteors in the Earth's Atmosphere*, 189–214.
- Grebowsky, J. M., & Brinton, H. C. (1978). Fe<sup>+</sup> ions in the high latitude F-region. *Geophysical Research Letters*, *5*(9), 791–794. <https://doi.org/10.1029/GL005i009p00791>
- Haldoupis, C., Pancheva, D., Singer, W., Meek, C., & MacDougall, J. (2007). An explanation for the seasonal dependence of midlatitude sporadic E layers. *Journal of Geophysical Research*, *112*, A06315. <https://doi.org/10.1029/2007JA012322>
- Haldoupis, C., Schlegel, K., & Farley, D. T. (1996). An explanation for type 1 radar echoes from the midlatitude E-region ionosphere. *Geophysical Research Letters*, *23*(1), 97–100. <https://doi.org/10.1029/95GL03585>
- Hanson, W. B., & Sanatani, S. (1971). Relationship between Fe<sup>+</sup> ions and equatorial spread F. *Journal of Geophysical Research*, *76*(31), 7761–7768. <https://doi.org/10.1029/JA076i031p07761>
- Huang, C. S., Miller, C. A., & Kelley, M. C. (1994). Basic properties and gravity wave initiation of the midlatitude F region instability. *Radio Science*, *29*(1), 395–405. <https://doi.org/10.1029/93RS01669>
- Huang, W., Chu, X., Gardner, C. S., Carrillo-Sánchez, J. D., Feng, W., Plane, J. M. C., & Nesvorniy, D. (2015). Measurements of the vertical fluxes of atomic Fe and Na at the mesopause: Implications for the velocity of cosmic dust entering the atmosphere. *Geophysical Research Letters*, *42*(1), 169–175. <https://doi.org/10.1002/2014GL062390>
- Huang, W. Q., Xiao, Z., Xiao, S. G., Zhang, D. H., Hao, Y. Q., & Suo, Y. C. (2011). Case study of apparent longitudinal differences of spread F occurrence for two midlatitude stations. *Radio Science*, *46*(1), RS1015. <https://doi.org/10.1029/2009RS004327>
- Huba, J. D., Krall, J., & Drob, D. (2019). Global ionospheric metal ion transport with SAMI3. *Geophysical Research Letters*, *46*(14), 7937–7944. <https://doi.org/10.1029/2019GL083583>
- Huba, J. D., Krall, J., & Drob, D. (2020). Modeling the impact of metallic ion layers on equatorial spread with SAMI3/ESF. *Geophysical Research Letters*, *47*(5), e2020GL087224. <https://doi.org/10.1029/2020GL087224>
- Istomin, V. G. (1963). Ions of extra-terrestrial origin in the Earth's ionosphere. *Planetary and Space Science*, *11*(2), 173–174. [https://doi.org/10.1016/0032-0633\(63\)90140-5](https://doi.org/10.1016/0032-0633(63)90140-5)
- Jiao, J., Chu, X., Jin, H., Wang, Z., Xun, Y., Du, L., et al. (2022). First lidar profiling of meteoric Ca<sup>+</sup> ion transport from ~80 to 300 km in the midlatitude nighttime ionosphere (Version 2). [Dataset]. Zenodo Data. <https://doi.org/10.5281/zenodo.7020759>
- Kelley, M. C. (2009). *The Earth's ionosphere: Plasma physics and electrodynamics*. Academic press.
- Kelley, M. C., & Fukao, S. (1991). Turbulent upwelling of the mid-latitude ionosphere 2. Theoretical framework. *Journal of Geophysical Research*, *96*(A3), 3747–3753. <https://doi.org/10.1029/90JA02252>
- Kelley, M. C., Makela, J. J., Chau, J. L., & Nicolls, M. J. (2003). Penetration of the solar wind electric field into the magnetosphere/ionosphere system. *Geophysical Research Letters*, *30*(4), 2002GL016321. <https://doi.org/10.1029/2002GL016321>
- Kopp, E. (1997). On the abundance of metal ions in the lower ionosphere. *Journal of Geophysical Research*, *102*(A5), 9667–9674. <https://doi.org/10.1029/97JA00384>
- MacDougall, J. W., Plane, J. M. C., & Jayachandran, P. T. (2000). Polar cap sporadic-E: Part 2, modeling. *Journal of Atmospheric and Solar-Terrestrial Physics*, *62*(13), 1169–1176. [https://doi.org/10.1016/S1364-6826\(00\)00092-4](https://doi.org/10.1016/S1364-6826(00)00092-4)
- Makela, J. J., & Otsuka, Y. (2012). Overview of nighttime ionospheric instabilities at low-and mid-latitudes: Coupling aspects resulting in structuring at the mesoscale. *Space Science Reviews*, *168*(1), 419–440. <https://doi.org/10.1007/s11214-011-9816-6>
- Mathews, J. (1998). Sporadic E: Current views and recent progress. *Journal of Atmospheric and Solar-Terrestrial Physics*, *60*(4), 413–435. [https://doi.org/10.1016/S1364-6826\(97\)00043-6](https://doi.org/10.1016/S1364-6826(97)00043-6)
- Nygren, T., Jalonen, L., Oksman, J., & Turunen, T. (1984). The role of electric field and neutral wind direction in the formation of sporadic E-layers. *Journal of Atmospheric and Terrestrial Physics*, *46*(4), 373–381. [https://doi.org/10.1016/0021-9169\(84\)90122-3](https://doi.org/10.1016/0021-9169(84)90122-3)
- Perkins, F. (1973). Spread F and ionospheric currents. *Journal of Geophysical Research*, *78*(1), 218–226. <https://doi.org/10.1029/JA078i001p00218>
- Plane, J. M. C. (2003). Atmospheric chemistry of meteoric metals. *Chemical Reviews*, *103*(12), 4963–4984. <https://doi.org/10.1021/cr0205309>
- Plane, J. M. C. (2012). Cosmic dust in the Earth's atmosphere. *Chemical Society Reviews*, *41*(19), 6507–6518. <https://doi.org/10.1039/c2cs35132c>
- Plane, J. M. C., Feng, W., & Dawkins, E. C. M. (2015). The mesosphere and metals: Chemistry and changes. *Chemical Reviews*, *115*(10), 4497–4541. <https://doi.org/10.1021/cr500501m>
- Plane, J. M. C., Feng, W., Gómez Martín, J. C., Gerding, M., & Raizada, S. (2018). A new model of meteoric calcium in the mesosphere and lower thermosphere. *Atmospheric Chemistry and Physics*, *18*(20), 14799–14811. <https://doi.org/10.5194/acp-18-14799-2018>
- Raizada, S., Smith, J. A., Lautenbach, J., Aponte, N., Perillat, P., Sulzer, M., & Mathews, J. D. (2020). New lidar observations of Ca<sup>+</sup> in the mesosphere and lower thermosphere over Arecibo. *Geophysical Research Letters*, *47*(5), e2020GL087113. <https://doi.org/10.1029/2020GL087113>
- Raizada, S., Tepley, C. A., Aponte, N., & Cabassa, E. (2011). Characteristics of neutral calcium and Ca<sup>+</sup> near the mesopause, and their relationship with sporadic ion/electron layers at Arecibo. *Geophysical Research Letters*, *38*(9), 2011GL047327. <https://doi.org/10.1029/2011GL047327>
- Raizada, S., Tepley, C. A., Williams, B. P., & García, R. (2012). Summer to winter variability in mesospheric calcium ion distribution and its dependence on sporadic E at Arecibo. *Journal of Geophysical Research*, *117*, A02303. <https://doi.org/10.1029/2011JA016953>
- Roddy, P. A., Earle, G. D., Swenson, C. M., Carlson, C. G., & Bullett, T. W. (2004). Relative concentrations of molecular and metallic ions in midlatitude intermediate and sporadic-E layers. *Geophysical Research Letters*, *31*(19), L19807. <https://doi.org/10.1029/2004GL020604>

- Roddy, P. A., Earle, G. D., Swenson, C. M., Carlson, C. G., & Bullett, T. W. (2007). The composition and horizontal homogeneity of E region plasma layers. *Journal of Geophysical Research*, *112*, A06312. <https://doi.org/10.1029/2006JA011713>
- Scharringhausen, M. (2007). *Investigation of mesospheric and thermospheric magnesium species from space*. Ph.D. thesis. Universität Bremen. Retrieved from <http://nbn-resolving.de/urn:nbn:de:gbv:46-diss000108346>
- Tsuda, T. T., Chu, X., Nakamura, T., Ejiri, M. K., Kawahara, T. D., Yukimatu, A. S., & Hosokawa, K. (2015). A thermospheric Na layer event observed up to 140 km over Syowa Station (69.0°S, 39.6°E) in Antarctica. *Geophysical Research Letters*, *42*(10), 3647–3653. <https://doi.org/10.1002/2015GL064101>
- Tsunoda, R. T. (1998). On polarized frontal structures, type-1 and quasi-periodic echoes in midlatitude sporadic E. *Geophysical Research Letters*, *25*(14), 2641–2644. <https://doi.org/10.1029/98GL01934>
- Tsunoda, R. T., & Cosgrove, R. B. (2001). Coupled electrodynamics in the nighttime midlatitude ionosphere. *Geophysical Research Letters*, *28*(22), 4171–4174. <https://doi.org/10.1029/2001GL013245>
- Vallance-Jones, A. (1956). Ca II emission lines in the twilight spectrum. *Nature*, *178*(4527), 276–277. <https://doi.org/10.1038/178276a0>
- Wei, L., Jiang, C., Hu, Y., Aa, E., Huang, W., Liu, J., et al. (2021). Ionosonde observations of spread F and spread Es at Low and middle latitudes during the recovery phase of the 7–9 September 2017 geomagnetic storm. *Remote Sensing*, *13*(5), 1010. <https://doi.org/10.3390/rs13051010>
- Wu, F., Zheng, H., Cheng, X., Yang, Y., Li, F., Gong, S., et al. (2020). Simultaneous detection of the Ca and Ca<sup>+</sup> layers by a dual-wavelength tunable lidar system. *Applied Optics*, *59*(13), 4122–4130. <https://doi.org/10.1364/AO.381699>
- Xun, Y., Yang, G., She, C. Y., Wang, J., Du, L., Yan, Z., et al. (2019). The first concurrent observations of thermospheric Na layers from two nearby central midlatitude lidar stations. *Geophysical Research Letters*, *46*(4), 1892–1899. <https://doi.org/10.1029/2018GL081645>
- Yokoyama, T., & Hysell, D. L. (2010). A new midlatitude ionosphere electrodynamics coupling model (MIECO): Latitudinal dependence and propagation of medium-scale traveling ionospheric disturbances. *Geophysical Research Letters*, *37*(8), L08105. <https://doi.org/10.1029/2010GL042598>
- Yokoyama, T., Hysell, D. L., Otsuka, Y., & Yamamoto, M. (2009). Three-dimensional simulation of the coupled Perkins and Es-layer instabilities in the nighttime midlatitude ionosphere. *Journal of Geophysical Research*, *114*(A3), A03308. <https://doi.org/10.1029/2008JA013789>
- Yuan, W., Xu, J., Ma, R., Wu, Q., Jiang, G., Gao, H., et al. (2010). First observation of mesospheric and thermospheric winds by a Fabry-Perot interferometer in China. *Chinese Science Bulletin*, *55*(35), 4046–4051. <https://doi.org/10.1007/s11434-010-4192-2>